



# Compositional control of tunnel features in hollandite-based ceramics: structure and stability of $(\text{Ba,Cs})_{1.33}(\text{Zn,Ti})_8\text{O}_{16}$

R. Grote<sup>1</sup> , M. Zhao<sup>1</sup> , L. Shuller-Nickles<sup>2,6</sup> , J. Amoroso<sup>3</sup> , W. Gong<sup>4</sup> , K. Lilova<sup>4</sup> , A. Navrotsky<sup>4</sup> , M. Tang<sup>5</sup> , and K. S. Brinkman<sup>1,6,\*</sup>

<sup>1</sup>Department of Materials Science and Engineering, Clemson University, Clemson, SC, USA

<sup>2</sup>Department of Environmental Engineering and Earth Sciences, Clemson, SC 29634, USA

<sup>3</sup>Savannah River National Laboratory, Aiken, SC 29808, USA

<sup>4</sup>University of California Davis, Davis, CA 95616, USA

<sup>5</sup>Los Alamos National Laboratory, Los Alamos, NM 87545, USA

<sup>6</sup>Center for Nuclear Environmental Engineering Sciences and Radioactive Waste Management (NEESRWM), Clemson University, Clemson, SC, USA

Received: 1 August 2018

Accepted: 5 September 2018

© Springer Science+Business Media, LLC, part of Springer Nature 2018

## ABSTRACT

The impact of composition on the tunnel features of hollandite materials for the purpose of radioactive cesium (Cs) immobilization was evaluated. The barium (Ba) to cesium (Cs) ratio was varied in the tunnel sites referred to as the A-site of the hollandite structure. Zinc (Zn) was substituted for titanium (Ti) on the B-site to achieve the targeted stoichiometry with a general formula of  $\text{Ba}_x\text{Cs}_y\text{Zn}_{x+y/2}\text{Ti}_{8-x-y/2}\text{O}_{16}$  ( $0 < x < 1.33$ ;  $0 < y < 1.33$ ). The tunnel cross-section depended on the average A-site cation radius, while the tunnel length depended on the average B-site cation radius. Substitution of Cs resulted in a phase transition from a monoclinic to a tetragonal structure and an increase in unit cell volume of 1.8% across the compositional range. Cs loss due to thermal evaporation was found to decrease in compositions with higher Cs content. The enthalpies of formation from binary oxides of Zn-doped hollandite measured using high-temperature oxide melt solution calorimetry were strongly negative, indicating thermodynamic stability with respect to their parent oxides. The formation enthalpies became more negative, indicating hollandite formation is more energetically favorable, when Cs was substituted for Ba across the range of Zn-doped compositions investigated in this study. Compositions with high Cs content exhibited lower melting points of approximately 80 °C. In addition, high Cs content materials exhibited a significant reduction in Cs release from the solid to liquid phase by leaching or aqueous corrosion as compared to low Cs content materials. These property changes would be beneficial for applications in radioactive cesium immobilization in a multi-phase ceramic by allowing for

Address correspondence to E-mail: ksbrink@clemson.edu

<https://doi.org/10.1007/s10853-018-2904-1>

Published online: 17 September 2018

Springer

decreased processing temperatures and higher cesium weight loadings. More broadly, these results establish the link between composition, structural symmetry, and thermodynamic stability for tunnel structured ceramics with implications in the design of new energy conversion and storage materials.

## Abbreviations

SYNROC Synthetic rock  
PCT Product consistency test

## List of symbols

$r_A$  Average radius of atoms on A-site  
 $r_B$  Average radius of atoms on B-site  
 $r_O$  Radius of oxygen  
 $t_H$  Tolerance factor  
 $Z_B$  Valence of B cation  
 $\delta_A$  Excess size of A cation  
 $\delta_B$  Excess size of B cation

## Introduction

Crystalline ceramics have been proposed as an alternative to glass as an immobilization matrix (i.e., waste form) for disposal of nuclear waste due to the enhanced retention of radionuclides in hydrothermal environments compared to current aluminoborosilicate glasses [1–4]. Crystalline ceramic waste forms were pioneered by Ringwood and others in the late 1970s [5]. Ceramic waste forms are generically termed SYNROC, a portmanteau of “synthetic rock” as they are designed to mimic geologically stable minerals assemblages. SYNROC typically consists of a multi-phase composite of distinct crystalline phases, each of which is compositionally tailored to immobilize specific elements or isotopes by chemical incorporation into the crystalline lattice. Hollandite is the mineral phase most often selected to immobilize Cs in the various SYNROC formulations. However, there are several key challenges associated with immobilizing Cs. Firstly, Cs isotopes are a major contributor to the heat generated and ionizing radiation produced during the first few hundred years of storage, requiring thermally stable materials systems [6]. Secondly, Cs is a large cation requiring coordination with eight nearest neighbors. This situation typically occurs in model crystalline phases such as

the CsCl structure [7]. The atomic size and water solubility of common Cs containing phases has driven research toward more complex structures such as hollandites, pollucites, glass and glass ceramics for Cs immobilization [3, 8–10].

In SYNROC, the hollandite phase is a limiting factor for system performance due to its lower radiation tolerance, higher leaching rate, and lower suggested waste loading of 5% [11]. For these reasons, considerable work has been performed on the stability, waste loading, and radiation tolerance of hollandite for Cs immobilization [2, 4, 12, 13]. This study explores the impact of varying A-site Cs stoichiometry of Zn-doped hollandites with the formula  $Ba_xCs_yZn_{x+y/2}Ti_{8-x-y/2}O_{16}$  ( $0 < x < 1.33$ ;  $0 < y < 1.33$ ). Specifically, this work examines the impact of Cs content on the hollandite structure, the melting point, the thermodynamic of formation and the aqueous leaching rates. Additionally, these compositions provide an opportunity to explore the effects of Zn, which is a minor component of the waste stream and has a larger ionic radius and lower valence ( $Zn^{2+}$ ) as compared to other dopants in the hollandite system ( $M^{3+}$  on the B-site such as  $Fe^{3+}$ ,  $Al^{3+}$ ,  $Ga^{3+}$  [11, 13]). These properties can be used to optimize scalable processing methods, such as melt and crystallization, as well as aid in the compositional development of resilient ceramic waste forms.

## Background

Hollandite<sup>1</sup> has the general formula  $A_2B_8O_{16}$ , where A is either mono- or divalent and B is di-, tri-, or tetravalent [5]. A wide range of substitutional compositions are possible due to the structural flexibility

<sup>1</sup> It is worth noting that for the purposes of this work, hollandite ( $BaMn_8O_{16}$ ) refers to hollandite-type structures which, are generically classified under a mineralogical hollandite supergroup consisting of Mn(IV) and Ti(IV) oxides distinguished by tunneled structures with tetragonal or pseudo-tetragonal crystal symmetry.

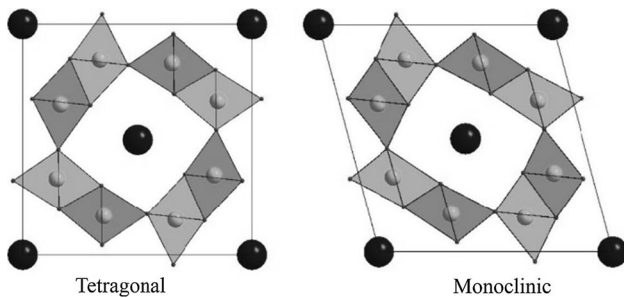


**Figure 1** Hollandite unit cell viewed down the  $c$ -axis (tunnel-direction) where tetragonal is  $(a = b) \neq c$  and monoclinic is  $(a \neq b) \neq c$ . The dark balls represent the A-site (Ba, Cs), the gray balls represent the B-site (Zn, Ti) and oxygen is on each corner of the tetrahedrons.

[4, 11, 14–21]. In Fig. 1, the two structural forms of hollandite are shown: tetragonal ( $I4/m$ ) and monoclinic ( $I2/m$ ) [22, 23]. The hollandite structure is based on pairs of edge-sharing  $\text{BO}_6$  octahedra extending along the short crystallographic axis. These  $\text{BO}_6$  pairs share corners with neighboring  $\text{BO}_6$  pairs forming a tunnel framework, which accommodates the larger A-site cations. The tunnel size can be altered by changing the A-site and/or B-site cations [13]. Several mechanisms can be used to compensate for the charge imbalance induced by doping  $\text{Cs}^{1+}$  on the  $\text{Ba}^{2+}$  site: including i)  $\text{Ti}^{4+}$  reducing to  $\text{Ti}^{3+}$  and ii)  $\text{Ti}^{4+}$  partially replacing a lower valent B-site cation,  $\text{M}^{3+/2+}$ . Substituting large cations on the B-site, such as Zn, will increase the tunnel size and unit cell volume providing more space for Cs storage. [11, 24–26]. Additionally, there is higher deformation of the  $a/b$  plane when doping larger cations on the A-site [24, 27, 28]. When a larger cation, such as Cs, is added to the composition,  $r_B$  decreases resulting in less B–B cation repulsion and smaller octahedra. One way to compensate for the increased  $r_A$  is by a distortion of the  $\text{BO}_6$  octahedra and expansion of the  $a/b$  plane. The causal relationship for  $a/b$  plane expansion is not fully understood; however,  $\text{BO}_6$  octahedral distortion has been reported for hollandites analyzed under pressure [24, 29].

Between 2004 and 2006, a Cs-loaded Zn-doped hollandite  $(\text{Ba,Cs})_{1.2}(\text{Zn,Ti})_8\text{O}_{16}$ , was synthesized and found to have relatively high Cs leach resistance; however, compositions with high Cs content were reported to be unstable and were unable to be synthesized [1, 30, 31]. Zn-based hollandites have also been investigated as high dielectric constant

materials with a range of Ba/Sr substitutions on the A-site [32]. In recent work by Xu et al., a complete solid solution has been demonstrated for Ga-doped hollandite of the form  $\text{Ba}_x\text{Cs}_y\text{Ga}_{2x+y}\text{Ti}_{8-2x-y}\text{O}_{16}$  ( $0 < x < 1.33$ ;  $y = 1.33 - x$ ), which exhibited tetragonal symmetry across the full solid solution. A solid solution across the A-site compositional range has not been observed to date in Zn-doped hollandites.

Scalable processing techniques, such as melting and crystallization require knowledge of the compositionally dependent melting points of candidate materials. To date, there have been limited studies on the melting point of Ba-hollandite. Some studies have investigated the B-site dopant effect on melting point, as well as the effluent gas composition and crystallization temperature [11, 12, 33]. The melting point data from the studies listed in Table 2 show that the melting point depends primarily on the B-site cations in the compositional ranges studied. Samples by Carter et al. were melt processed and contained less than 65% hollandite with melting points that were 100–200 °C lower than [33]. In work by Costa et al., precursor powders formed single phase hollandite with melting data close to values published by Aubin et al. [11, 12, 33]. Understanding the dopant effects on the melting point and elemental volatility will aid in developing methods for efficient large-scale processing techniques.

The structural stability of hollandite is governed by the interplay between the ionic radius, cation repulsion, tunnel cation ordering, cation occupancy and cation the valence. Post et al. (1982) developed a simple ratio rule, where  $r_B$  refers to the average B cation radii and  $r_A$  refers to the average A cation radii. Post's rule states that when  $r_B/r_A < 0.48$  the structure will be tetragonal. However, this rule does not address the number (or valence) of cations and uses the average cation size, which ought to be accounted for when determining structural stability. Kesson et al. (1986) showed that a tolerance factor, called  $t_H$  was based on the average A-site cation radii,  $r_A$ , average B-site cation radii,  $r_B$ , and oxygen radius,  $r_O$ , could be used to predict the propensity for hollandite phase formation. In this framework, an ideal tetragonal structure would have a  $t_H = 1$ , while  $t_H$  values ranging from 0.93 to 1.16 were predicted to form a stable hollandite phase [23]. Drawbacks of this model include not accounting for octahedral distortions, ordering, or symmetry as it relies entirely on ionic radii.

$$t_H = \frac{[(r_A + r_O)^2 - 1/2(r_B + r_O)^2]^{1/2}}{\sqrt{3/2}(r_B + r_O)} \quad (1)$$

Building on the prior work of Post, Zhang et al. (1994) derived a more complete equation for predicting unit cell length and symmetry. Geometrical considerations and atomic level data including the valence of the B cation,  $Z_B$ , and the excess size of the cations,  $\delta_A$  and  $\delta_B$ , were used to derive equations for the lattice constant,  $a$ , and the  $c$  lattice constant,  $c$ . These calculations were based on 55 compositions collected from literature, most of which had fully occupied A-site compositions containing Ba (no Cs).

$$a(\text{\AA}) = 5.130(r_O + r_B) - 0.291Z_B + 0.441\delta_A \quad (2)$$

$$c(\text{\AA}) = \sqrt{2}(r_O + r_B) - 0.0366Z_B + 0.552\delta_B \quad (3)$$

These equations present a correlation between the tunnel cation size and the structural symmetry of the compound. Three distinct symmetry regions were also identified: tetragonal symmetry, monoclinic symmetry, or undetermined symmetry. Undetermined regions correspond to the space between tetragonal and monoclinic symmetry; in this region the symmetry was determined by octahedral distortions and ordering effects [24]. The current work will show that occupancy plays a role in symmetry stability.

The durability, or resistance to elemental release, is a measure of a waste form's performance and utility as a host for mobile radionuclides, such as Cs. Two methods were used for quantifying elemental release in this work: (1) the ASTM C 1285 product consistency test (PCT), which measures elemental release from crushed powder at elevated temperature, and (2) the ASTM C 1220 leach test, which measures elemental release from a monolith at an elevated temperature. The PCT (and ASTM C 1220) have been used globally as standardized leach tests for compositional screening [34, 35].

## Experimental methods

Hollandite samples of the general formula  $Ba_xCs_yZn_{2x+y}Ti_{8-2x-y}O_{16}$ , where  $x$  ranged from 0 to 1.333 and  $y = 1.333 - x$ , were synthesized from reagent grade oxides and carbonates by solid state reaction in air. This study will discuss nine compositions, five of

which are denoted as Ba133, Cs029, Cs067, Cs100, and Cs133 and four which were used for calorimetry, Cs015, Cs043, Cs029 (ExCs), and Cs133 (ExCs) all of which are listed in Table 1. Those listed with (ExCs) contained 15% excess Cs atoms prior to calcination. The precursor powders were ball milled in ethanol and calcined for 10 h at 1225 °C. The powders were subsequently ball milled and calcined a second time for 10 h at 1225 °C. Calcined powders were ball milled and pressed into pellets (335 MPa) followed by sintering at 1300 °C for 1 h.

Structure and elemental composition were characterized by XRD with Cu  $K\alpha$  wavelength ( $\lambda = 1.54 \text{ \AA}$ ) with a Rigaku Ultima IV and refined using the FullProf software. SEM and EDX were collected with a S-3400N VP-SEM. TEM micrographs were imaged at ANL with a 300 keV Hitachi 9000. Weight percent of secondary phases were sufficiently low as to be within the XRD error. Therefore, the secondary phase weight percent was calculated by averaging the area of rutile per total area of SEM images.

Thermogravimetric analysis (TGA) was performed using a Perkin Elmer TGA 7 to record from 25 to 1000 °C at 10 °C/min and 1000 °C to 1250 °C at 5 °C/min. Differential Scanning Calorimetry (DSC) was performed using a Netzsch DSC 404 C to measure from 25 to 1450 °C on 6–10 mg samples in yttrium-coated alumina crucibles at 10 °C/min with 60 mL/min argon flow. Infrared (IR-spectroscopy) was performed with a Thermo-Nicolet Magna 550 FTIR after samples were calcined at four different temperatures; 350 °C, 650 °C, 800 °C and 1050 °C. The melting points were calculated from the onset of the endothermic peak.

High-temperature oxide melt solution calorimetry was performed using the AlexSYS 1000 calorimeter (SETARAM) operating at 702 °C with sodium molybdate ( $3Na_2O \cdot 4MoO_3$ ) solvent to measure enthalpies of formation of six different Zn-doped hollandites. Detailed instrument and experimental procedure can be found in reviews and reports by Navrotsky [36, 37]. Approximately 5–10 mg samples were weighted, loosely pressed into pellets and dropped from room temperature into the molten oxide solvent contained in a platinum crucible in the calorimeter. The calorimeter assembly was flushed with gas at an average of 50 mL/min rate. Gas was also bubbled through the solvent at 5 mL/min in order to stir the melt and enhance the dissolution rate of the samples. Since there is no change in the

**Table 1** Target, EDX and ICP-MS compositions with refined lattice constants

Target composition	EDX composition	ICP-MS	Acronym	Lattice constants a; (b); c
Ba <sub>1.333</sub> Zn <sub>1.333</sub> Ti <sub>6.667</sub> O <sub>16</sub>	Ba <sub>1.306</sub> Cs <sub>0.000</sub> Zn <sub>1.360</sub> Ti <sub>6.667</sub> O <sub>16</sub>	–	Ba133*	10.175; (10.077); 2.970
Ba <sub>1.040</sub> Cs <sub>0.293</sub> Zn <sub>1.187</sub> Ti <sub>6.814</sub> O <sub>16</sub>	Ba <sub>1.057</sub> Cs <sub>0.210</sub> Zn <sub>1.210</sub> Ti <sub>6.814</sub> O <sub>16</sub>	Ba <sub>1.077</sub> Cs <sub>0.196</sub> Zn <sub>1.200</sub> Ti <sub>6.814</sub> O <sub>16</sub>	Cs029	10.133; 2.979
Ba <sub>0.667</sub> Cs <sub>0.667</sub> Zn <sub>1.000</sub> Ti <sub>7.000</sub> O <sub>16</sub>	Ba <sub>0.672</sub> Cs <sub>0.581</sub> Zn <sub>1.037</sub> Ti <sub>7.000</sub> O <sub>16</sub>	Ba <sub>0.694</sub> Cs <sub>0.559</sub> Zn <sub>1.026</sub> Ti <sub>7.000</sub> O <sub>16</sub>	Cs067*	10.187; 2.971
Ba <sub>0.333</sub> Cs <sub>1.000</sub> Zn <sub>0.834</sub> Ti <sub>7.166</sub> O <sub>16</sub>	Ba <sub>0.311</sub> Cs <sub>0.941</sub> Zn <sub>0.887</sub> Ti <sub>7.166</sub> O <sub>16</sub>	–	Cs100	10.220; 2.969
Cs <sub>1.333</sub> Zn <sub>0.667</sub> Ti <sub>7.333</sub> O <sub>16</sub>	Ba <sub>0.000</sub> Cs <sub>1.268</sub> Zn <sub>0.700</sub> Ti <sub>7.333</sub> O <sub>16</sub>	Ba <sub>0.025</sub> Cs <sub>1.199</sub> Zn <sub>0.709</sub> Ti <sub>7.333</sub> O <sub>16</sub>	Cs133	10.254; 2.962
Ba <sub>1.18</sub> Cs <sub>0.153</sub> Zn <sub>1.257</sub> Ti <sub>6.743</sub> O <sub>16</sub>	Ba <sub>1.100</sub> Cs <sub>0.134</sub> Zn <sub>1.347</sub> Ti <sub>6.743</sub> O <sub>16</sub>	–	Cs015*	–
Ba <sub>1.040</sub> Cs <sub>0.293</sub> Zn <sub>1.187</sub> Ti <sub>6.814</sub> O <sub>16</sub>	Ba <sub>1.048</sub> Cs <sub>0.260</sub> Zn <sub>1.195</sub> Ti <sub>6.814</sub> O <sub>16</sub>	–	Cs029 (ExCs)*	–
Ba <sub>0.90</sub> Cs <sub>0.43</sub> Zn <sub>1.117</sub> Ti <sub>6.883</sub> O <sub>16</sub>	Ba <sub>0.830</sub> Cs <sub>0.427</sub> Zn <sub>1.190</sub> Ti <sub>6.883</sub> O <sub>16</sub>	–	Cs043*	–
Cs <sub>1.333</sub> Zn <sub>0.667</sub> Ti <sub>7.333</sub> O <sub>16</sub>	Ba <sub>0.000</sub> Cs <sub>1.320</sub> Zn <sub>0.673</sub> Ti <sub>7.333</sub> O <sub>16</sub>	–	Cs133 (ExCs)*	–

Cs029 (ExCs) and Cs133 (ExCs) contained 15% excess Cs to counteract Cs loss during processing. \*Samples used for calorimetry all other tests used the first five compositions

oxidation state of the ions after dissolution, either air or oxygen can be used for flushing and bubbling. Measurements were repeated at least six times (should be 8 successful drops or 6 only if the error is below 1%) to achieve statistically reliable data. The real composition based on EDX measurements were used for all calculations. The calorimeter was calibrated using the heat content of  $\alpha$ -alumina.

Two methods were used for quantifying elemental release: (1) the ASTM C 1285 product consistency test (PCT) which uses particles and (2) the ASTM C 1220 leach test, which uses a monolithic specimen. For the ASTM C 1285 tests, the PCT-A procedure was followed. Each composition was measured in triplicate using  $\sim 1.5$  g of washed and sieved ( $-100/+200$  mesh) powder in  $\sim 15$  mL of de-ionized water. For the ASTM C 1220 tests, each composition was measured in duplicate using monolithic samples approximately 8 mm  $\times$  8 mm  $\times$  2 mm in de-ionized water ( $\sim 15$  mL) to maintain a constant surface area to volume (S/V) ratio of 13 mm<sup>2</sup>/mL between all samples. In addition to the samples, two blanks and a standard reference material referred to as the approved reference material (ARM) was prepared in triplicate for the PCT testing. All samples and standards were loaded into sealed stainless steel pressure vessels, sealed with threaded enclosures, and heated at  $\sim 90$  °C for  $\sim 7$  days. Subsequently, the vessels were cooled and the leachates were filtered, acidified, and measured for elemental composition using inductively coupled plasma mass spectrometry (ICP-MS). The concentration of elements in the leachates were compared to the elemental concentrations in the

un-leached samples that were measured using ICP-MS from excess washed and sieved powder (from PCT preparation) to obtain a fraction loss for each element.

## Results and discussion

Initial screening experiments for Zn-doped samples showed that an A-site occupancy ranges from 63 to 83% readily formed hollandite with no secondary phases which was in agreement with the existing knowledge for stability ranges. A compositional range was designed to avoid A-site occupancy effects; therefore, the occupancy was held constant at 67% to allow for comparisons with published data in similar systems [11, 27, 38]. The 67% occupancy was selected to create solid solutions with integer values of A-site dopants for a limited supercell which was amenable to DFT modeling performed in prior work [22, 38, 39]. Five compositions, referred to as, Ba133, Cs029, Cs067, Cs100, and Cs133, were prepared to test the range of hollandite stability with corresponding variations in Zn/Ti ratio in order to charge balance the structure. The XRD patterns of the synthesized hollandite samples are shown in Fig. 2. All compositions were identified as  $I4/m$  (tetragonal) hollandite and found good agreement with published powder diffraction data for Ba<sub>0.41</sub>Cs<sub>0.82</sub>Ti<sub>8</sub>O<sub>16</sub> (PDF# 080-2264) except for the pure Ba composition (Ba133), which was  $I2/m$  (monoclinic) and agreed well with Ba<sub>1.31</sub>Ti<sub>8</sub>O<sub>16</sub> (PDF# 080-0910) [40]. Overall, the patterns indicate the samples were single phase and

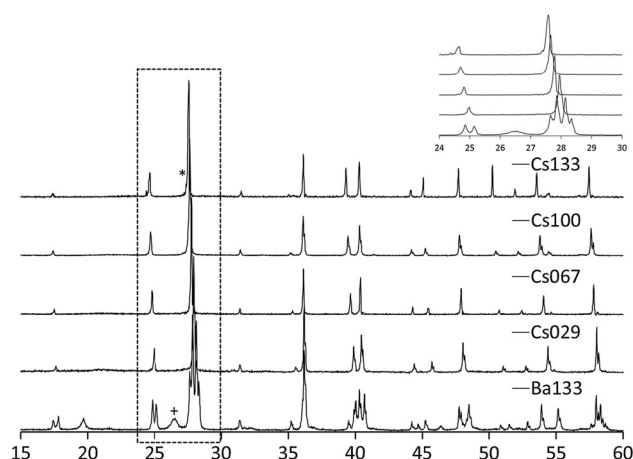


**Figure 2** XRD patterns of  $\text{Ba}_x\text{Cs}_y\text{Zn}_{x-y/2}\text{Ti}_{8-x+y/2}\text{O}_{16}$  synthesized by oxide route after sintering to 1300 °C for 1 h with Cs = 0.00, 0.29, 0.67, 1.00, 1.33. PDF# 080-2264 and 020-0910 were used to identify the tetragonal and monoclinic symmetry \* denotes rutile ( $\text{TiO}_2$ ) and + denotes tunnel ordering.

crystalline. However, a minor peak at about  $27.3^\circ$  corresponding to rutile was visible in the Cs133 pattern. In addition, a broad peak in the Ba133 pattern at  $26.5^\circ$  has been attributed to tunnel ordering which is also observed in existing hollandite literature [41, 42]. A minor amount of rutile in the otherwise single phase hollandite has been observed in prior work and likely results from excess Ti, possibly due to Cs volatilization [1]. The XRD patterns exhibited a shift in the primary hollandite peak near  $28^\circ$  as a function of composition. The primary peak shifted toward lower  $2\theta$  (Fig. 2) with increasing Cs content, which indicates an increased unit cell volume. The observed volume expansion was primarily attributed to differences in the A-site cation size of Cs ( $r_{\text{Cs}} = 1.74 \text{ \AA}$ ) versus Ba ( $r_{\text{Ba}} = 1.42 \text{ \AA}$ ). Structural data showing the volume expansion increased linearly with the average A-site radius indicated this effect was due to tunnel expansion rather than B-site octahedral expansion. Figure 3a compares the  $a$  and  $c$  lattice parameters as a function of Cs concentration and shows that the tunnel cross-section expansion is an order of magnitude greater than the tunnel length expansion. The trends in the calculated values for  $a$  and  $c$  lattice parameters as a function of Cs concentration based on Eq. 2 generally agree with measured results. The differences which do exist between the experimental and model predictions could be due to partial occupancy of the current samples ranging from 62 to 65%. Model predictions outlined in Eq. 2

assume full tunnel occupancy with a tetragonal structure [24].

The decrease observed in the  $c$  lattice parameter with increased Cs content was attributed to the reduction in the average B-site cation radius ( $\text{Ti}^{4+}$  replaces  $\text{Zn}^{2+}$  as Cs content increases). After fully substituting Cs on the tunnel sites, the lattice expanded 1.2% along the  $a$ -axis and contracted 0.6% along the  $c$ -axis, resulting in a total volume expansion of 1.8%. The unit cell deformation results agree with previously reported trends in a Ga hollandite system [24, 27, 28]. Figure 3b compares the samples from this study to the Post and Zhang structural equations. It shows that the Ba end member, which formed monoclinic, was within the undetermined zone, while the other compositions formed tetragonal as predicted. The 67% partial A-site occupancy and large Zn substitutions are probably what allowed for a monoclinic symmetry to form. In addition to confirming the lattice expansion trends for Zn-doped hollandite over the A-site solid solution previously seen in the Ga system, the current work demonstrates how composition can control the symmetry.

Figure 4 displays the SEM determined microstructure of the sintered hollandites. Minor  $\text{TiO}_2$  formation, identified by XRD and EDX, and increased grain size were observed with increasing Cs content. No rutile was observed by SEM (or measured by XRD) in Cs029, whereas the rutile content increased to 1 and 4 weight percent for Cs067 and Cs133, respectively. TEM selected area electron diffraction patterns (SAED) were collected to confirm monoclinic symmetry in the Ba133 composition and tetragonal symmetry in the Cs029, Cs067 and Cs133 compositions as observed in XRD. Overall, these results indicate a trend that increasing Cs content results in the stabilization of the tetragonal symmetry and an expansion of the unit cell. Stabilization of the tetragonal symmetry occurred below Cs029, with 67% occupancy, for the Zn-doped hollandite.

### Thermal analysis

Cs loss upon volatilization is a known phenomenon when processing hollandite at high temperatures and has been quantified ex-situ through pre- and post-processing compositional analysis; however, it has not been well quantified for hollandite materials [13, 17, 43, 44]. The effect of targeted Cs stoichiometry on Cs retention during high temperature processing

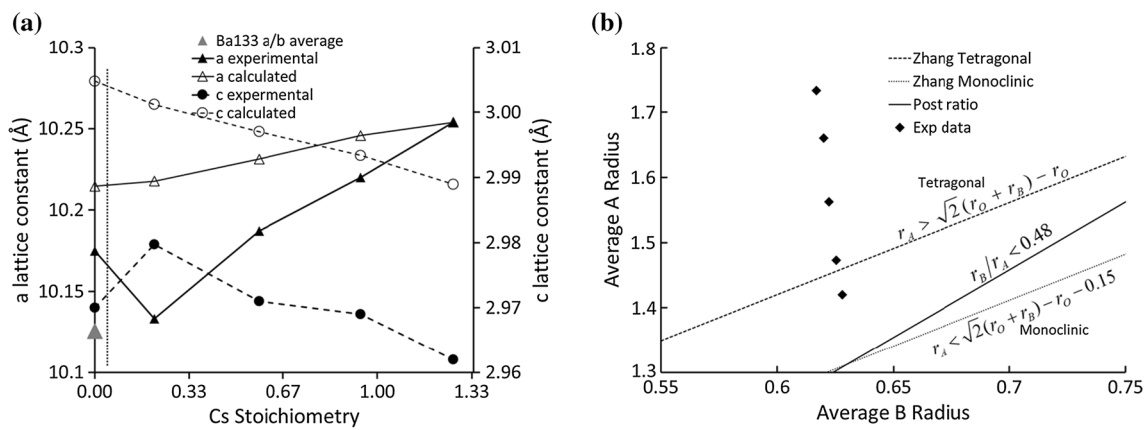


**Figure 3** **a** Lattice constants dependence on Cs stoichiometry. The vertical dashed line at Cs 0.29 denotes the approximate monoclinic to tetragonal boundary; **b** stability predictions for experimental data based on geometrical calculations by Zhang and Post.

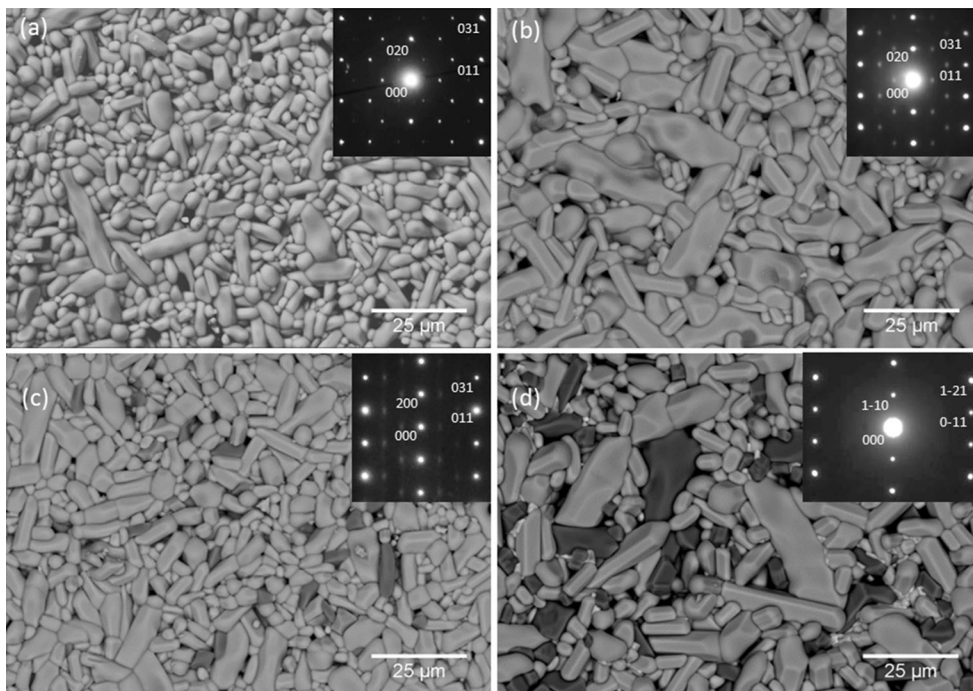


**Figure 4** Backscatter electron micrographs (BSE) of unpolished hollandite grains **a** Ba133; **b** Cs029; **c** Cs067; **d** Cs133. The dark grains are TiO<sub>2</sub>, as indicated by EDX, and the light grains are the

hollandite. The TEM patterns for Ba133, Cs029, Cs067, and Cs133 were along the [100], [100], [100], and [111] zone axes respectively.

is of practical and theoretical interest. TGA measurements were performed on samples of precursor powder to quantify the mass loss of Cs for each composition during heating. There should be no significant difference between Ba116, Ba<sub>1.16</sub>Zn<sub>1.16</sub>Ti<sub>6.84</sub>O<sub>16</sub>, and Ba133 as both form the same structure and neither contain Cs. Four distinct temperature zones in which weight loss occurred are shown in

Fig. 5. The first zone from 0 to 300 °C was associated with desorption of water and CO<sub>2</sub> [26]. The second zone near 550 °C was attributed to the decomposition of Cs<sub>2</sub>CO<sub>3</sub> to Cs<sub>2</sub>O. The third zone starting at 800 °C can be attributed to the loss of carbonate from the BaCO<sub>3</sub> precursor. As a reference for this analysis, pure Ba compositions exhibited no mass loss in the second zone, while the pure Cs compositions

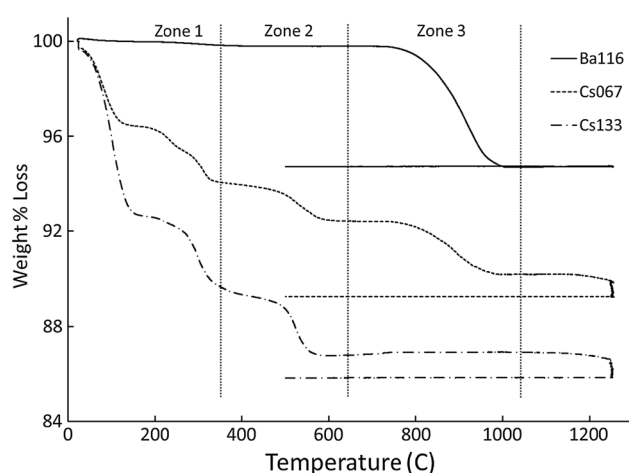


**Figure 5** TGA scan of ZnTi hollandite from 20 to 1250 °C weight loss from each zone was attributed to a different process, Zone 1: H<sub>2</sub>O evaporation, Zone 2: Cs<sub>2</sub>CO<sub>3</sub> decomposition and Zone 3: BaCO<sub>3</sub> decomposition.

exhibited no mass loss across the third zone. The fourth zone at 1250 °C, the sintering temperature, exhibited mass loss attributed to Cs volatilization. Cs<sub>2</sub>O has the lowest decomposition temperature and SEM–EDX elemental analysis indicated Cs exhibited the greatest deviation from target stoichiometry.

The decomposition reactions for each temperature regime seen in TGA were confirmed by ATR-FTIR. Results from the FTIR characterization revealed significant differences between the three samples Ba133, Cs067 and Cs133 after 350, 650 and 800 °C heat treatments. The primary feature used to identify structural changes was the Cs<sub>2</sub>CO<sub>3</sub> major peak at

1334 cm<sup>-1</sup> and minor peak at 1440 cm<sup>-1</sup>. The relative intensity of BaCO<sub>3</sub> peaks was also used; however, the TiO<sub>2</sub> peaks overlapped with the BaCO<sub>3</sub> peak at 1421 cm<sup>-1</sup> and all the ZnO vibrational modes were below the measured range. After the 350 °C heat treatment, a significant difference in peak intensity was observed for the BaCO<sub>3</sub> and Cs<sub>2</sub>CO<sub>3</sub> peaks as seen in Fig. 6a. Figure 6b displays the spectra at 800 °C, indicating the Cs<sub>2</sub>CO<sub>3</sub> fully decomposed as the vibrations associated with BaCO<sub>3</sub> remained in the spectra. All the precursors were reacted at temperatures in excess of 1050 °C as seen in Fig. S2. The remaining peaks were associated with hollandite vibrational modes below 800 cm<sup>-1</sup>. The comparison of the 350, 800 and 1050 °C data showed that Cs<sub>2</sub>CO<sub>3</sub> was more reactive than BaCO<sub>3</sub> since it decomposed at a lower temperature and confirms Cs<sub>2</sub>CO<sub>3</sub> as the first carbonate precursor to decompose during the TGA experiment.

Analysis of the isothermal hold at 1250 °C indicated that mass loss increased with increasing Cs content as shown in Fig. 7. However, normalized Cs mass loss, defined by dividing the Cs mass loss by the initial Cs mass in the sample calculated from material stoichiometry exhibited a different trend. The normalized Cs mass loss decreased with increasing initial Cs content. The decreased relative Cs mass loss indicates that hollandite formation was more favorable with higher Cs content, and that the resulting structures were more stable with regard to high-temperature Cs loss. This conclusion agrees with the XRD results indicating that the tetragonal

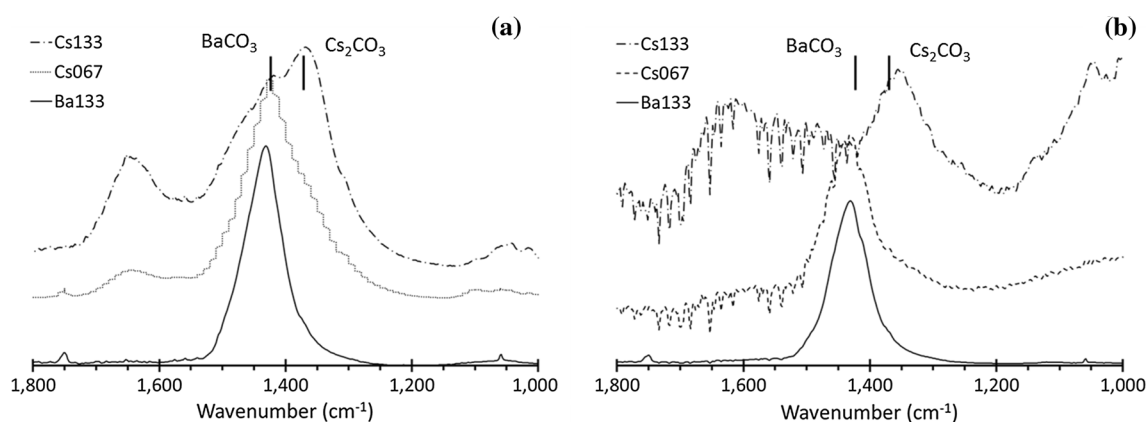


**Figure 6** **a** FTIR after 350 °C calcination; **b** FTIR after 800 °C calcination. The TiO<sub>2</sub> peaks overlap with the BaCO<sub>3</sub> peak at 1421 cm<sup>-1</sup>, while the Cs<sub>2</sub>CO<sub>3</sub> has a major peak at 1334 cm<sup>-1</sup> and

a minor peak at 1440 cm<sup>-1</sup>. ZnO vibration modes do not have peaks within the 1000 cm<sup>-1</sup> to 1800 cm<sup>-1</sup> range.

phase stability increased with additional Cs content and supports the hypothesis that increased rutile formation is due to higher amounts of Cs evaporation.

## DSC

Table 2 displays the melting points measured by DSC, which were observed to decrease with increasing Cs content and average B-site radii. The melting point depression has been previously associated with Cs doping [11]. However, in this work, Cs substitution was shown to result in melting point depressions of about 80 °C, which is comparable to melting point changes between different B-site doped systems [11, 12, 33]. However, there are a number of other factors that affect the melting point therefore the average B-site radii is not a reliable predictor for melting point changes. Zn hollandite had melting points below Cr-hollandite and similar to Fe- and Al-

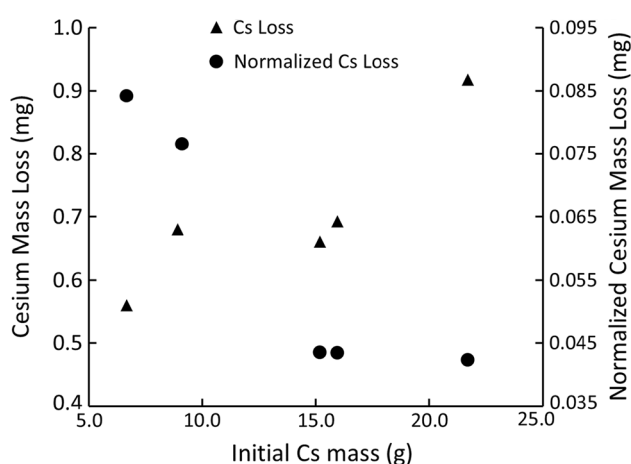


**Figure 7** Cesium (Cs) mass loss and Normalized Cesium (Cs) mass loss as determined from TGA experiments. Normalized Cs mass loss was calculated by dividing the total Cs mass loss by the initial Cs mass in the sample determined by stoichiometry.

doped hollandite. There were also endothermic peaks near 550 °C and 800 °C that agree with the TGA decomposition analysis.

## Calorimetry

Table 3 gives a summary of the measured enthalpies of drop solution ( $\Delta H_{ds}$ ) for six different hollandites. Using these  $\Delta H_{ds}$  values (shown in Table 4 and Fig. 8a) and previous reported  $\Delta H_{ds}$  and  $\Delta H_{f,el}$  data for BaO, Cs<sub>2</sub>O, ZnO and TiO<sub>2</sub> (shown in Table 3), enthalpies of formation for six hollandite phases from their constituent oxides ( $\Delta H_{f,ox}$ ) and from elements ( $\Delta H_{f,el}$ ) were calculated via thermochemical cycles using the real (EDX) composition. The thermochemical cycle for a general compound Ba<sub>x</sub>Cs<sub>y</sub>Zn<sub>x+y/2</sub>Ti<sub>8-x-y/2</sub>O<sub>16</sub> is shown in Table 5. The obtained  $\Delta H_{f,ox}$  and  $\Delta H_{f,el}$  are also listed in Table 3. As shown in Table 3 and Fig. 8b, the values of  $\Delta H_{f,ox}$  of all six hollandite compositions were strongly exothermic, indicating that they are thermodynamically stable relative to their constituent oxides. Moreover, these values become more negative (more exothermic) with increasing Cs content. This decreasing trend agreed with the DFT modeling results for Zn hollandite [45].

Even though large exothermic formation enthalpies of six Zn-doped hollandites indicate their strong thermodynamic stability relative to their binary constituent oxides, one must consider their stability with respect to other competing phase assemblages, including ternary constituent oxides, when evaluating the hollandite suitability as a nuclear waste form [12]. A potential phase assemblage may contain BaTiO<sub>3</sub> (perovskite) and other constituent oxides, which can be assessed by thermodynamics using the following reactions (analyzed EDX stoichiometries are used as examples) [12]:



**Table 2** Reported melting points for different M<sup>2+/3+</sup> doped hollandite and ZnTi hollandite melting points calculated from onset measurements of the endothermic peak

Author	Composition/melting point (°C)		
Carter [33]	Ba(Mn/Ti)O/1315 °C	Ba(Fe/Ti)O/1350 °C	Ba(Cr/Ti)O/1450 °C
Costa [12]	Ba <sub>1.24</sub> Al <sub>2.28</sub> Ti <sub>5.52</sub> O <sub>16</sub> /1427 °C	Ba <sub>1.24</sub> Mg <sub>1.12</sub> Ti <sub>6.76</sub> O <sub>16</sub> /1477 °C	Ba <sub>1.24</sub> Fe <sub>2.28</sub> Ti <sub>5.52</sub> O <sub>16</sub> /1481 °C
Aubin [11]	Ba <sub>1.16</sub> Fe <sub>2.32</sub> Ti <sub>6.68</sub> O <sub>16</sub> /1447 °C	Ba <sub>1.16</sub> Al <sub>2.32</sub> Ti <sub>6.68</sub> O <sub>16</sub> /1517 °C	Ba <sub>1.16</sub> Cr <sub>2.32</sub> Ti <sub>6.68</sub> O <sub>16</sub> /1650 °C
This work	Ba133/1379 °C    Cs029/1361 °C	Cs067/1359 °C    Cs100/1336 °C	Cs133/1299 °C

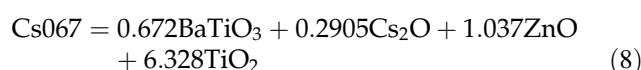
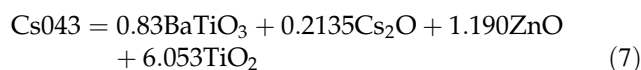
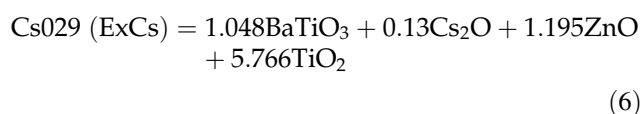
**Table 3** Enthalpies of drop solution ( $\Delta H_{ds}$ ) in sodium molybdate solvent at 702 °C and enthalpies of formation from component oxides ( $\Delta H_{f,ox}$ ) and from the elements ( $\Delta H_{f,el}$ ) of four hollandite phases at 25 °C

Target phase	$\Delta H_{ds}$ (kJ/mol)	$\Delta H_{f,ox}$ (kJ/mol), EDX	$\Delta H_{f,el}$ (kJ/mol), EDX
Ba133	$370.54 \pm 4.32$ (8)	$-179.84 \pm 6.14$	$-7665.98 \pm 8.59$
Cs015	$380.99 \pm 7.67$ (8)	$-171.26 \pm 8.53$	$-7634.87 \pm 10.36$
Cs029 (ExCs)	$399.66 \pm 5.73$ (8)	$-200.95 \pm 6.74$	$-7671.60 \pm 8.95$
Cs043	$405.50 \pm 6.97$ (8)	$-191.58 \pm 7.56$	$-7635.02 \pm 9.52$
Cs067	$422.44 \pm 6.18$ (6)	$-202.07 \pm 6.65$	$-7642.37 \pm 8.82$
Cs133 (ExCs)	$444.46 \pm 3.66$ (8)	$-219.39 \pm 3.94$	$-7606.26 \pm 7.12$

Uncertainty is two standard deviation of the mean and value in parentheses is the number of experiments

**Table 4** Enthalpies of drop solution in sodium molybdate solvent at 702 °C ( $\Delta H_{ds}$ ) and enthalpies of formation from the elements ( $\Delta H_{f,el}$ ) at 25 °C of related component binary oxides

Oxide	$\Delta H_{ds}$ (kJ/mol)	$\Delta H_{f,el}$ (kJ/mol)
BaO	$-184.61 \pm 3.21^2$	$-548.1 \pm 2.1^6$
Cs <sub>2</sub> O	$-348.9 \pm 1.7^3$	$-346.0 \pm 1.2^6$
ZnO	$19.4 \pm 0.7^4$	$-350.5 \pm 0.3^6$
TiO <sub>2</sub>	$60.81 \pm 0.11^5$	$-944.0 \pm 0.8^6$



Cs–Zn–O, Cs–Ti–O and Zn–Ti–O could theoretically form additional phases, but they have not been reported in SYNROC. In addition, enthalpies of formation are not available for many of these potential phases and will not be considered in the subsequent analysis. The enthalpies of reaction ( $\Delta H_{rxn}$ ) at standard conditions are calculated as follows [12, 15]:

$$\begin{aligned} \Delta H_{rxn,(\text{Ba133}-\text{EDX})} &= 1.306\Delta H_{f,ox}(\text{BaTiO}_3) - \Delta H_{f,ox}(\text{Ba133}-\text{EDX}) \\ &= -19.07 \pm 8.96 \text{ kJ/mol} \end{aligned}$$

$$\begin{aligned} \Delta H_{rxn,(\text{Cs015}-\text{EDX})} &= 1.10\Delta H_{f,ox}(\text{BaTiO}_3) - \Delta H_{f,ox}(\text{Cs015}-\text{EDX}) \\ &= 3.73 \pm 10.20 \text{ kJ/mol} \end{aligned}$$

$$\begin{aligned} \Delta H_{rxn,(\text{Cs029(ExCs)}-\text{EDX})} &= 1.048\Delta H_{f,ox}(\text{BaTiO}_3) - \Delta H_{f,ox}(\text{Cs029(ExCs)}-\text{EDX}) \\ &= 41.34 \pm 8.12 \text{ kJ/mol} \end{aligned}$$

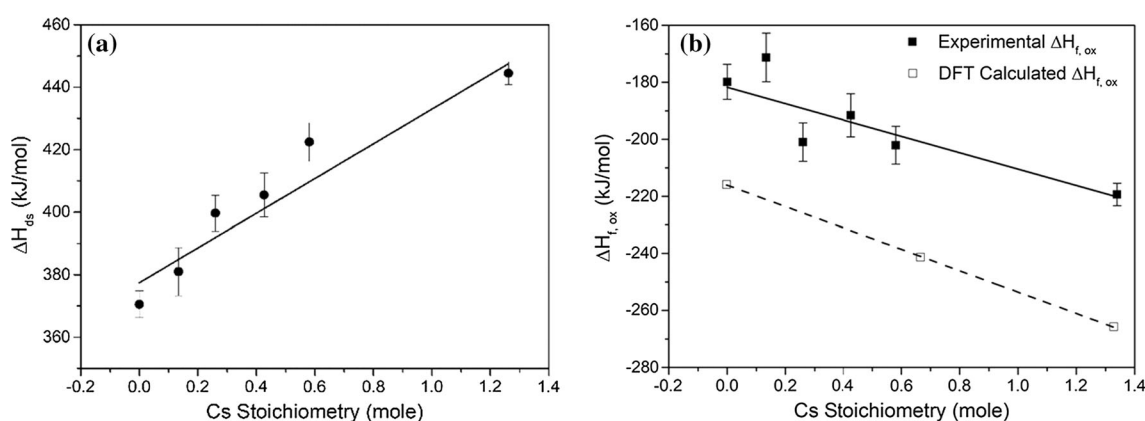


**Figure 8** **a** Drop solution enthalpy,  $\Delta H_{ds}$ , across the Zn hollandite compositional range increased with increasing Cs content; **b** experimental enthalpies of formation and DFT calculated enthalpies versus Cs stoichiometry from the

component oxides at 25 °C ( $\Delta H_{f,ox}$ ) for Zn hollandite decreased (formation became more favorable) with increasing Cs content [45].

**Table 5** Thermochemical cycle for the general compound  $Ba_xCs_yZn_{x+y/2}Ti_{8-x-y/2}O_{16}$  that was used for calculation of enthalpies of formation hollandite from constituent oxides ( $\Delta H_{f,ox}$ ) and from the elements ( $\Delta H_{f,el}$ ) at 25 °C with correction based on EDX analyzed composition in Table 1

Enthalpy of formation of $Ba_xCs_yZn_{x+y/2}Ti_{8-2x-y/2}O_{16}$ from the oxides at 25 °C ( $\Delta H_{f,ox}$ )	
$Ba_xCs_yZn_{2x+y}Ti_{8-2x-y}O_{16}(s,25^\circ C) \rightarrow xBaO(sln,702^\circ C) + y/2Cs_2O(sln,702^\circ C) + 2x+yZnO(sln,975 K) + 8-2x-yTiO_2(sln,702^\circ C)$	$\Delta H_{ds}$
$BaO(s,298 K) \rightarrow BaO(sln,702^\circ C)$	$\Delta H_1$
$Cs_2O(s,298 K) \rightarrow Cs_2O(sln,702^\circ C)$	$\Delta H_2$
$ZnO(s,298 K) \rightarrow ZnO(sln,702^\circ C)$	$\Delta H_3$
$TiO_2(s,298 K) \rightarrow TiO_2(sln,702^\circ C)$	$\Delta H_4$
$xBaO(s,298 K) + y/2Cs_2O(s,25^\circ C) + 2x+yZnO(s,25^\circ C) + 8-2x-yTiO_2(s,25^\circ C) \rightarrow Ba_xCs_yZn_{2x+y}Ti_{8-2x-y}O_{16}(s,25^\circ C)$	$\Delta H_{f,ox}$
Enthalpy of formation of $Ba_xCs_yZn_{x+y/2}Ti_{8-2x-y/2}O_{16}$ from the elements at 25 °C ( $\Delta H_{f,el}$ )	
$xBaO(s,298 K) + y/2Cs_2O(s,25^\circ C) + 2x+yZnO(s,25^\circ C) + 8-2x-yTiO_2(s,25^\circ C) \rightarrow Ba_xCs_yZn_{2x+y}Ti_{8-2x-y}O_{16}(s,25^\circ C)$	$\Delta H_{f,ox}$
$Ba(s,298 K) + 1/2O_2(g,25^\circ C) \rightarrow BaO(s,25^\circ C)$	$\Delta H_5$
$1/2Cs(s,298 K) + 1/2O_2(g,25^\circ C) \rightarrow Cs_2O(s,702^\circ C)$	$\Delta H_6$
$Zn(s,298 K) + 1/2O_2(g,25^\circ C) \rightarrow ZnO(s,702^\circ C)$	$\Delta H_7$
$Ti(s,298 K) + O_2(g,25^\circ C) \rightarrow TiO_2(s,702^\circ C)$	$\Delta H_8$
$xBa(s,298 K) + yCs(s,25^\circ C) + 2x+yZn(s,25^\circ C) + 8-2x-yTi(s,25^\circ C) + 8O_2(g,25^\circ C) \rightarrow Ba_xCs_yZn_{2x+y}Ti_{8-2x-y}O_{16}(s,25^\circ C)$	$\Delta H_{f,el}$

$$\Delta H_{rxn,(Cs043-EDX)} = 0.83\Delta H_{f,ox}(BaTiO_3) - \Delta H_{f,ox}(Cs043-EDX) = 65.17 \pm 7.44 \text{ kJ/mol}$$

$$\Delta H_{rxn,(Cs067-EDX)} = 0.672\Delta H_{f,ox}(BaTiO_3) - \Delta H_{f,ox}(Cs067-EDX) = 99.72 \pm 6.00 \text{ kJ/mol}$$

where  $\Delta H_{f,ox}$  values of hollandite are from Table 3,  $\Delta H_{f,ox}(BaTiO_3) = -152.3 \pm 4.0 \text{ kJ/mol}$ .

The Cs end member was not calculated as it contains no Ba to form  $BaTiO_3$ . Therefore based on the  $\Delta H_{rxn}$  of five hollandites it can be concluded that Cs029 (ExCs), Cs043, and Cs067 are energetically stable at room temperature with respect to  $BaTiO_3$ ,  $Cs_2O$ ,  $ZnO$ , and  $TiO_2$ , as their  $\Delta H_{rxn}$  are endothermic. In contrast, Ba133 is not stable with respect to  $BaTiO_3$ ,  $ZnO$ , and  $TiO_2$ , as determined by the exothermic  $\Delta H_{rxn}$ . Moreover, the stability of Cs015 was comparable to that of  $BaTiO_3$ ,  $ZnO$ , and  $TiO_2$ , because its reaction enthalpy was close to zero considering experimental uncertainties. The thermochemical analysis further supports that increased Cs substitution stabilizes the hollandite phase from the perspective of formation enthalpy of the targeted phase, as well as from possible decomposition to other phases.

### Leaching measurements

The calculated fractional release of Cs for individual replicates from the particle and monolith leach testing is summarized in Fig. 9. For the PCT (particle) samples, the fraction of Cs released decreased as Cs stoichiometry (concentration) was increased. This behavior indicates that the Cs stoichiometry in hollandite affects its release, which is supported by reported favorable formation enthalpies and structural stabilization caused by increasing Cs stoichiometry [13]. Similar behavior was observed for the monolith samples although there was greater variability among replicates with lower Cs stoichiometry. More striking, however, was the similar magnitude in the calculated fraction release of Cs from the monoliths compared to the particles. Both the variance in replicate response and the nominal fraction of Cs release could be attributed to several factors including pH, microstructure, and surface area. The measured pH values after testing were measured and although variation was seen, experience indicates that the effect would not be significant. Therefore,

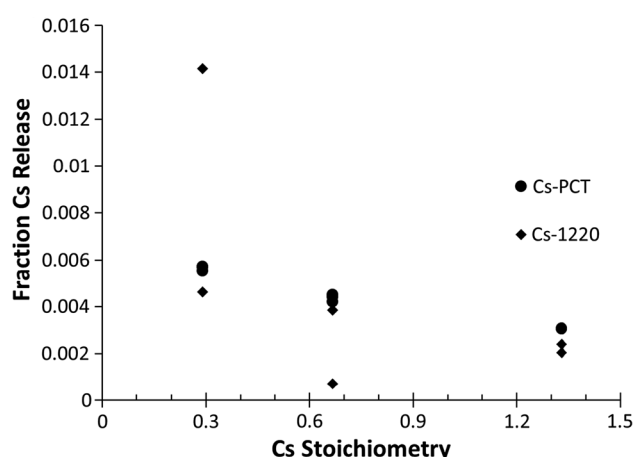


**Figure 9** Fraction of Cs released from PCT and C 1220 leaching measurements for Cs029, Cs067 and Cs133 compositions; Circle: PCT measurements of Cs leaching Diamond: C 1220 measurements of Cs leaching.

surface area measurements using the Brunauer–Emmett–Teller method (Micromeritics) were performed on the Cs067 monolith samples post-leaching and confirmed that the surface area was several hundred times greater than if geometrically estimated, which could explain the data. The variance in the leach data for the monolith replicates also appeared to increase with decreasing Cs stoichiometry. Although XRD and SEM analysis indicated the samples were phase homogeneous, the replicate variance could indicate that surface area is not the only contributing factor, but phase/structure formation also impacts the Cs leaching behavior, further supporting the supposition that increasing Cs stoichiometry in hollandite is favorable for formation and stability. The fraction release of Ba and Zn elements were on the order of  $10^{-4}$  and  $10^{-5}$ , respectively, for all replicates.

## Conclusion

Solid state processing was utilized to synthesize  $\text{Ba}_x\text{Cs}_y\text{Zn}_{x+y/2}\text{Ti}_{8-x-y/2}\text{O}_{16}$  in order to examine the effect of Cs and Zn substitutions on the structure, thermal properties, and resistance to aqueous corrosion of the resulting hollandite materials. Cs additions led to a structural shift from a monoclinic to a more stable tetragonal phase which was accompanied by unit cell expansion. Cs was also found to further stabilize the tetragonal structure across the solid solution as seen by reductions in Cs loss during heating, a decrease in Cs released during aqueous

leaching tests, and lower formation enthalpies. High Cs content hollandites resulted in lowered melting points which could limit Cs evaporation and facilitate large-scale processing. In summary, Cs-rich hollandite compositions are more favorable to form, resulting in a stable structure with enhanced Cs retention. More broadly, these results establish the link between composition, structural symmetry, and thermodynamic stability for tunnel structured ceramics with implications in the design of new energy conversion and storage materials.

## Acknowledgements

KSB and MZ acknowledge support of thermodynamic measurements as part of the Center for Hierarchical Waste Form Materials, an Energy Frontier Research Center funded by the U.S. Department of Energy, Office of Science, Basic Energy Sciences under Award No. DE-SC0016574. LSN gratefully acknowledges financial support from the DOE-EPSCoR Project Number: DE-SC0012530, “Radionuclide Waste Disposal: Development of Multi-scale Experimental and Modeling Capabilities” for support of modeling. The calorimetric experiments carried out at University of California, Calorimetry at Davis were supported as part of the Materials Science of Actinides, an Energy Frontier Research Center funded by the U.S. Department of Energy, Office of Science, Basic Energy Sciences under Award Number DE-SC0001089. JA acknowledges the support of durability testing by the U.S. Department of Energy, Office of Nuclear Energy, Fuel Cycle Technology, Materials Recovery and Waste Form Development Campaign. Work conducted at Savannah River National Laboratory was supported by the U.S. Department of Energy under contract number DE-AC09-08SR22470.

## Compliance with ethical standards

**Conflict of interest** K. Brinkman is a member of the editorial board for Journal of Materials Science. The authors declare that they have no other conflict of interest.

**Electronic supplementary material:** The online version of this article (<https://doi.org/10.1007/s10853-018-2904-1>) contains supplementary material, which is available to authorized users.

## References

- [1] Carter ML, Vance ER, Li H (2004) Hollandite-rich ceramic melts for the immobilisation of Cs. *MRS Proc.* <https://doi.org/10.1557/PROC-807-249>
- [2] Carter ML, Vance ER (2008) HIPed tailored ceramic waste forms for the immobilisation of Cs, Sr and Tc. *MRS Proc.* <https://doi.org/10.1557/PROC-1107-323>
- [3] Ringwood AE, Kesson SE, Ware NG et al (1979) Immobilisation of high level nuclear reactor wastes in SYNROC. *Nat J* 278:219–223
- [4] Tang M, Tumurugoti P, Clark B et al (2016) Heavy ion irradiations on synthetic hollandite-type materials: Ba<sub>1.0</sub>Cs<sub>0.3</sub>A<sub>2.3</sub>Ti<sub>5.7</sub>O<sub>16</sub> (A = Cr, Fe, Al). *J Solid State Chem* 239:58–63. <https://doi.org/10.1016/j.jssc.2016.04.014>
- [5] Ringwood AE, Kesson SE, Ware NG et al (1979) The SYNROC process: a geochemical approach to nuclear waste immobilization. *Geochem J* 13:141–165
- [6] Abdelouas A, Utsunomiya S, Suzuki T et al (2008) Effects of ionizing radiation on the hollandite structure-type: Ba<sub>0.85</sub>Cs<sub>0.26</sub>Al<sub>1.35</sub>Fe<sub>0.77</sub>Ti<sub>5.90</sub>O<sub>16</sub>. *Am Mineral* 93:241–247. <https://doi.org/10.2138/am.2008.2563>
- [7] Cheary RW (1986) An analysis of the structural character of hollandite compounds. *Acta Crystallogr Sect B Struct Sci* 42:229–236
- [8] Gombert D, Piet S, Trichel T et al (2008) Combined waste form cost trade study; INL/EXT-08-14993 (GNEPSYSA-PMO-MI-DV-2009-000003). Idaho National Laboratory, Idaho Falls, ID
- [9] Lee WE, Ojovan MI, Stennett MC, Hyatt NC (2006) Immobilisation of radioactive waste in glasses, glass composite materials and ceramics. *Adv Appl Ceram* 105:3–12. <https://doi.org/10.1179/174367606X81669>
- [10] Chen TY, Maddrell ER, Hyatt NC, Hriljac JA (2016) A potential wasteform for Cs immobilization: synthesis, structure determination, and aqueous durability of Cs<sub>2</sub>TiNb<sub>6</sub>O<sub>18</sub>. *Inorg Chem* 55:12686–12695. <https://doi.org/10.1021/acs.inorgchem.6b01826>
- [11] Aubin-Chevaldonnet V, Caurant D, Dannoux A et al (2007) Preparation and characterization of (Ba, Cs)<sub>x</sub>(M, Ti)<sub>8</sub>O<sub>16</sub> (M = Al<sup>3+</sup>, Fe<sup>3+</sup>, Ga<sup>3+</sup>, Cr<sup>3+</sup>, Sc<sup>3+</sup>, Mg<sup>2+</sup>) hollandite ceramics developed for radioactive cesium immobilization. *J Nucl Mater* 366:137–160. <https://doi.org/10.1016/j.jnucmat.2006.12.051>
- [12] Costa GCC, Xu H, Navrotsky A (2013) Thermochemistry of barium hollandites. *J Am Ceram Soc* 96:1554–1561. <https://doi.org/10.1111/jace.12224>
- [13] Xu Y, Wen Y, Grote R et al (2016) A-site compositional effects in Ga-doped hollandite materials of the form Ba<sub>x</sub>Cs<sub>y</sub>Ga<sub>2x+y</sub>Ti<sub>8-2x-y</sub>O<sub>16</sub>: implications for Cs immobilization in crystalline ceramic waste forms. *Sci Rep.* <https://doi.org/10.1038/srep27412>
- [14] Carter ML (2004) Tetragonal to monoclinic phase transformation at room temperature in Ba<sub>x</sub>Fe<sub>2x</sub>Ti<sub>8-2x</sub>O<sub>16</sub> hollandite due to increased Ba occupancy. *Mater Res Bull* 39:1075–1081. <https://doi.org/10.1016/j.materresbull.2004.02.018>
- [15] Xu H, Wu L, Zhu J, Navrotsky A (2015) Synthesis, characterization and thermochemistry of Cs-, Rb- and Sr-substituted barium aluminium titanate hollandites. *J Nucl Mater* 459:70–76. <https://doi.org/10.1016/j.jnucmat.2015.01.014>
- [16] Zandbergen HW, Everstijn PLA, Mijlhoff FC et al (1987) Composition, constitution and stability of the synthetic hollandites A<sub>x</sub>M<sub>4-2x</sub>N<sub>2x</sub>O<sub>8</sub>, M = Ti, Ge, Ru, Zr, Sn and N = Al, Sc, Cr, Ga, Ru, In and the system (A, Ba)<sub>x</sub>Ti<sub>y</sub>Al<sub>z</sub>O<sub>8</sub> with A = Rb, Cs, Sr. *Mater Res Bull* 22:431–438. [https://doi.org/10.1016/0025-5408\(87\)90252-2](https://doi.org/10.1016/0025-5408(87)90252-2)
- [17] Amoroso J, Marra JC, Tang M et al (2014) Melt processed multiphase ceramic waste forms for nuclear waste immobilization. *J Nucl Mater* 454:12–21. <https://doi.org/10.1016/j.jnucmat.2014.07.035>
- [18] Cheary RW, Squadrito R (1989) A structural analysis of barium magnesium hollandites. *Acta Crystallogr Sect B Struct Sci* 45:205–212. <https://doi.org/10.1107/S0108768188014053>
- [19] Xu Y, Grote R, Wen Y et al (2016) Development of Ga doped hollandites Ba<sub>x</sub>Cs<sub>y</sub>(Ga<sub>2x+y</sub>Ti<sub>8-2x-y</sub>)O<sub>16</sub> for Cs Immobilization. *Ceramics for energy conversion, storage, and distribution systems*. Wiley, Hoboken, pp 157–164
- [20] Brinkman KS, Amoroso J, Marra JC, Tang M (2013) Crystalline ceramic waste forms: comparison of reference process for ceramic waste form fabrication, SRNL-STI-2013-00442
- [21] Bystrom A, Bystrom AM (1950) The crystal structure of hollandite, the related manganese oxide minerals, and Alpha-MnO<sub>2</sub>. *ACTA Crystallogr* 3:146–154. <https://doi.org/10.1107/S0365110X5000032X>
- [22] Post JE, Von Dreele RB, Buseck PR (1982) Symmetry and cation displacements in hollandites: structure refinements of hollandite, cryptomelane and priderite. *Acta Crystallogr Sect B Struct Crystallogr Cryst Chem* 38:1056–1065. <https://doi.org/10.1107/S0567740882004968>
- [23] Kesson SE, White TJ (1986) Radius ratio tolerance factors and the stability of hollandites. *J Solid State Chem* 63:122–125. [https://doi.org/10.1016/0022-4596\(86\)90160-X](https://doi.org/10.1016/0022-4596(86)90160-X)
- [24] Zhang J, Burnham CW (1994) Hollandite-type phases: geometric consideration of unit-cell size and symmetry. *Am Mineral* 79:168–174
- [25] Haaker RF, Ewing RC (1981) Naturally occurring crystalline phases: analogues for radioactive waste forms, PNL-3505

- [26] Cai J, Liu J, Willis WS, Suib SL (2001) Framework doping of iron in tunnel structure cryptomelane. *Chem Mater*. <https://doi.org/10.1021/cm0014233>
- [27] Xu Y, Feyngenson M, Page K et al (2016) Structural evolution in hollandite solid solutions across the A-site compositional range from Ba<sub>1.33</sub>Ga<sub>2.66</sub>Ti<sub>5.34</sub>O<sub>16</sub> to Cs<sub>1.33</sub>Ga<sub>1.33</sub>-Ti<sub>6.67</sub>O<sub>16</sub>. *J Am Ceram Soc* 4106:4100–4106. <https://doi.org/10.1111/jace.14443>
- [28] Aubin-Chevaldonnet V, Badot JC, Caurant D (2007) The permittivity and the conductivity of Ba-hollandite Ba<sub>1.16</sub>M<sub>2.32</sub>Ti<sub>5.68</sub>O<sub>16</sub> (M = Al, Ga) observed by dielectric spectroscopy. *Solid State Ion* 178:1274–1281. <https://doi.org/10.1016/j.ssi.2007.06.016>
- [29] Zhang J, Ko J, Hazen R, Prewitt C (1993) High-pressure crystal chemistry of KAlSi<sub>3</sub>Or hollandite. *Am Mineral* 78:493–499
- [30] Carter ML, Jostsons A, Vance ER (2003) Hollandite containing ceramic, Australian Nuclear Science & Technology Organization. Patent Publication Number WO/2003/05864, 07/17/2003, International Application Number PCT/AU2003/000031
- [31] Hyatt NC, Stennett MC, Fiddy SG et al (2006) Synthesis and characterisation of transition metal substituted barium hollandite ceramics. *MRS Proc* 932(60):1. <https://doi.org/10.1557/PROC-932-60.1>
- [32] Remya R, Murali KP, Potty SN, Priyadarshini V (2005) Structure and dielectric properties of Ba<sub>1-x</sub>Sr<sub>x</sub> ZnTi<sub>7</sub>O<sub>16</sub> hollandite ceramics. *J Electron Mater* 34:1076–1080
- [33] Carter ML, Vance ER, Cassidy DJ et al (2004) Hollandite ceramics: effect of composition on melting temperature. *Ceram Trans* 168:207–216
- [34] Bibler NE, Jantzen CM (1989) The product consistency test and its role in the waste acceptance process for DWPF glass. *Manag Radioact Wastes Non-Radioactive Wastes from Nucl Facil* 743–749
- [35] Hench LL, Clark DE, Campbell J (1984) High level waste immobilization forms. *Nucl Chem Waste Manag* 5:149–173. [https://doi.org/10.1016/0191-815X\(84\)90045-7](https://doi.org/10.1016/0191-815X(84)90045-7)
- [36] Navrotsky A, Rock PA (2014) Progress and new directions in calorimetry: a 2014 perspective. *J Am Ceram Soc* 3359:3349–3359. <https://doi.org/10.1111/jace.13278>
- [37] Navrotsky A (1997) Progress and new directions in high temperature calorimetry revisited. *Phys Chem Miner* 24:222–241
- [38] Cheary RW, Squadrito R (1992) Electron and X-ray diffraction from antiphase domains in the barium magnesium hollandite Ba<sub>1.33</sub>Mg<sub>1.33</sub>Ti<sub>6.67</sub>O<sub>16</sub>. *Acta Crystallogr Sect A Found Crystallogr* 48:15–27. <https://doi.org/10.1107/S0108767391008668>
- [39] Aubin V, Caurant D, Gourier D et al (2003) Synthesis, characterization and study of the radiation effects on hollandite ceramics developed for cesium immobilization. *MRS Proc* 807:315–320. <https://doi.org/10.1557/PROC-807-315>
- [40] International Centre for Diffraction Data, Powder Diffraction File, Joint Committee on Powder Diffraction Standards, Philadelphia, PA, 1974–present
- [41] Cheary RW, Kwiatkowska J (1984) An X-ray structural analysis of cesium substitution in the barium hollandite phase of synroc. *J Nucl Mater* 125:236–243
- [42] Carter ML, Withers RL (2005) A universally applicable composite modulated structure approach to ordered Bax-MyTi<sub>8-y</sub>O<sub>16</sub> hollandite-type solid solutions. *J Solid State Chem* 178:1903–1914. <https://doi.org/10.1016/j.jssc.2005.03.040>
- [43] Amoroso JW, Marra J, Dandeneau CS et al (2017) Cold crucible induction melter test for crystalline ceramic waste form fabrication: a feasibility assessment. *J Nucl Mater* 486:283–297. <https://doi.org/10.1016/j.jnucmat.2017.01.028>
- [44] Amoroso J, Marra J, Conradson SD et al (2014) Melt processed single phase hollandite waste forms for nuclear waste immobilization: Ba<sub>1.0</sub>Cs<sub>0.3</sub>A<sub>2.3</sub>Ti<sub>5.7</sub>O<sub>16</sub>; A = Cr, Fe, Al. *J Alloys Compd* 584:590–599. <https://doi.org/10.1016/j.jallcom.2013.09.087>
- [45] Wen Y, Xu Y, Brinkman KS, Shuller-Nickles L (2018) Atomistic scale investigation of cation ordering and phase stability in Cs-substituted Ba<sub>1.33</sub>Zn<sub>1.33</sub>Ti<sub>6.67</sub>O<sub>16</sub>, Ba<sub>1.33</sub>Ga<sub>2.66</sub>Ti<sub>5.67</sub>O<sub>16</sub> and Ba<sub>1.33</sub>Al<sub>2.66</sub>Ti<sub>5.33</sub>O<sub>16</sub> hollandite. *Sci Rep* 8:1–11. <https://doi.org/10.1038/s41598-018-22982-7>